

Significant enhancement of critical current density in H⁺-intercalated FeSe single crystal

Yan Meng^{1,4}(孟炎), Wei Wei^{1,4}(魏伟), Xiangzhuo Xing^{1,2,3}(邢相灼), Xiaolei Yi¹(易晓磊), Nan Zhou¹(周楠), Yufeng Zhang¹(张宇丰), Wenhui Liu¹(刘雯慧), Yue Sun^{1,3}(孙悦), and Zhixiang Shi^{1,3}(施智祥)

¹ *School of Physics, Southeast University, Nanjing 211189, China*

² *School of Physics and Physical Engineering, Qufu Normal University, Shandong 273165, China*

³ Authors to whom any correspondence should be addressed. E-mail: xzxing@qfnu.edu.cn, sunyue@phys.aoyama.ac.jp and zxshi@seu.edu.cn

⁴ These authors contributed equally to this paper.

Abstract

Superconducting transition temperature (T_c) and critical current density (J_c) are two key factors that are not only crucial for probing high temperature superconducting mechanism, but also for practical applications. The simple crystal structure of FeSe is very favorable for the fabrication of thin films and wires, but its application is limited by the relatively low T_c and small J_c . Previous study has found that the T_c of FeSe can be significantly enhanced over 40 K by using protonation method. Here, we present a systematic study of J_c and vortex properties of H⁺-intercalated FeSe (H_x-FeSe) single crystals. The value of J_c for H_x-FeSe single crystal is significantly enhanced, exceeding 1.3×10^6 A/cm² at 4 K, which is more than two orders of magnitude larger than 1.1×10^4 A/cm² of pristine FeSe. The vortex pinning mechanism of H_x-FeSe is found to be surface pinning, which is different from the dominant strong point-like pinning in pristine FeSe. Moreover, the systematic study of the vortex phase transition and the underlying mechanism provides a wealth of information for the vortex phase diagram of H_x-FeSe single crystal. Our results confirm that the introduction of H⁺ intercalations into FeSe not only enhance the T_c , but also significantly increase the value of J_c , which is favorable for practical applications.

Keywords: H⁺-intercalated FeSe single crystal, protonation, critical current density, pinning mechanism, vortex phase diagram

1. Introduction

Amongst iron-based superconductors (IBSs), FeSe [1, 2], has attracted considerable interest because of its peculiar properties. One of the significant research subjects in FeSe is about the tunability and improvement of superconducting (SC) transition temperature T_c , which is crucial not only for probing high- T_c SC mechanism but also for practical applications. The T_c of the pristine FeSe single crystal is

only 9 K [1], while it can be dramatically increased by various methods. Among them, bulk superconductivity of T_c around 30 - 40 K has been realized by intercalating alkaline/alkali-earth metals [3-6], NH_3 [7-12], LiOH [13-16], and organic molecules [17-19] into FeSe layers. Another approach to achieve high T_c is based on the ionic liquid gating technique, which can precisely tune the carrier concentrations and improve the T_c of FeSe flakes or films up to 48 K [20, 21]. In addition, unusual discrete SC phases with maximum T_c of 44 K were obtained by a new solid ionic gating device, which can effectively drive Li^+/Na^+ ions into the bulk FeSe flakes [22].

To date, various methods have been proven to be efficient for achieving high- T_c superconductivity in FeSe. Nevertheless, for the high- T_c FeSe-derived superconductors, J_c and vortex pinning are the most vital properties in practical applications, which have not been widely studied. This is probably due to the limitations of the following unfavorable factors. For instance, both of K-coated and ionic liquid gating methods can only accumulate carriers on the subsurface of FeSe films due to the Thomas-Fermi screening effect [23]. Moreover, traditional gating method is processed by in situ electrical transport measurement at low temperatures with voltage, which brings difficulties to the subsequent post-gating measurements [20]. The instability and sensitivity of metal ions/organic molecules intercalated FeSe also hinder the study of J_c and vortex pinning [24]. Nevertheless, there are still some relevant reports in these high- T_c FeSe-derived superconductors. The largest J_c in $(\text{Li}_{1-x}\text{Fe}_x)\text{OHFeSe}$ single crystal reaches a value about $7 \times 10^5 \text{ A/cm}^2$ at 5 K [25, 26]. Some other studies on J_c have also been carried out in $\text{K}_x\text{Fe}_2\text{Se}_2$ [27, 28], $\text{Fe}(\text{Se},\text{Te})$ [29] and $\text{Li}_x(\text{NH}_3)_y\text{Fe}_2\text{Te}_{1.2}\text{Se}_{0.8}$ [30] single crystals.

Recently, Cui et al. reported the intercalation of proton (H^+) into the bulk materials such as IBSe by a protonation method [31-33], which successfully induces superconductivity or enhances T_c . The benefit of such method is that protons are not volatile, hence the protonated samples are relatively stable under ambient conditions, which provides the possibility and convenience for various subsequent measurements. Very recently, we reports a step-like SC phase diagram as a function of the electron concentrations in H^+ -intercalated FeSe single crystals [34]. The optimal SC phase of T_c^{onset} over 44 K are prepared, which provides an ideal platform to investigate J_c and vortex pinning of FeSe-derived superconductors.

In this study, we systematically studied the enhancement of J_c , vortex pinning, and vortex phase diagram in optimally protonated FeSe single crystal with $T_c \sim 44 \text{ K}$. The value of J_c for $\text{H}_x\text{-FeSe}$ is significantly enhanced over $1 \times 10^6 \text{ A/cm}^2$ at 4 K under self-field, which is more than two orders of magnitude higher than $1.1 \times 10^4 \text{ A/cm}^2$ of pristine FeSe [35, 36]. The pinning mechanism of $\text{H}_x\text{-FeSe}$ can be described by surface pinning, and the vortex glass state of tail region is investigated under the vortex glass theory model. Furthermore, flux pinning behavior and vortex liquid state properties are examined based on the thermally activated flux flow theory (TAFF). The detailed study of the vortex

phase transition and the underlying mechanism provides rich information for the vortex phase diagram of H_x -FeSe single crystals.

2. Experimental details

The pristine FeSe single crystals used for protonation were obtained by the chemical vapor transport growth [35, 37]. The selected high-quality single crystals were then cleaved into thin crystals of approximately 15 μm thickness, with a size of $720 \times 410 \times 15 \mu\text{m}^3$. The protonation configuration and process are described in detail in our recently published paper [34]. The optimal H_x -FeSe single crystal of T_c^{onset} over 44 K was obtained after 20 days' protonation. The same sample was used for the magnetic and electrical transport measurements. The powder and single-crystal x-ray diffraction results show that H^+ intercalation has negligible effect on the lattice structure of H_x -FeSe single crystals [34]. Magneto-transport measurements were performed on the Physical Property Measurement System (PPMS-9T) with an excitation current of 1 mA. Magnetic measurements were performed with the VSM option of the Physical Property Measurement System (PPMS-9T). The magnetic field sweeping rate was set to 120 Oe/s for magnetic hysteresis loops.

3. Results and discussion

The temperature dependences of resistivity and magnetization measurements are shown in Figs. 1(a) and (b) for pristine FeSe and H_x -FeSe single crystal, respectively. It is noted that the normal state resistivity behaviour in H_x -FeSe is similar to those of FeSe-derived superconductors such as $(\text{Li}_{1-x}\text{Fe}_x)\text{OHFeSe}$ [25] and $\text{Li}_x(\text{NH}_3)_y\text{Fe}_2\text{Se}_2$ [7], but is different from that of pristine FeSe, indicating the change of electronic structure and or scattering mechanism after protonation. The residual resistivity ratio (RRR), defined as $\rho(300 \text{ K})/\rho(0 \text{ K})$, is about 20 for H_x -FeSe, which is smaller than that of pristine FeSe (~ 70), indicating that more impurity scatterings are introduced simultaneously by H^+ intercalations. H_x -FeSe exhibits a SC transition temperature $T_c \sim 44 \text{ K}$, which is significantly higher than that of the pristine FeSe of $\sim 9 \text{ K}$. The inset of Fig. 1(b) shows the temperature dependence of field cooling (FC) and zero field cooling (ZFC) magnetization, manifesting that the optimal H_x -FeSe single crystal exhibits an almost 100% SC volume, indicating the nature of bulk property.

Magnetic hysteresis loops (MHLs) at different temperatures for FeSe and H_x -FeSe superconductors are measured and compared in Figs. 2(a) and (b). The symmetrical MHLs demonstrate the dominance of the bulk pinning in both samples. The second magnetization peaks are absent in all the loops, and M decreases monotonically with the increase of H . Such behaviour is quite different from other IBSs [38-42], but is consistent with the FeSe-derived superconductors [35, 36, 43]. The value of J_c can be derived from the MHLs by the extended Bean model [44], $J_c = 20\Delta M/[a(1 - a/3b)]$. Here ΔM [emu/cm^3] is the different value between the magnetization M_{up} of upward field sweep and magnetization M_{down} of downward field sweep. The a [cm] (width) and b [cm] (length) correspond to the size of the sample

($a < b$). J_c of FeSe and H_x -FeSe at different temperatures are illustrated in Figs. 2 (a) and (b), respectively. The derived J_c of H_x -FeSe single crystal reaches an extremely large value of 1.33×10^6 A/cm² under zero field at 4 K, which is more than two orders larger than that of the FeSe of 1.1×10^4 A/cm² [36, 37]. To the best of our knowledge, such value is one of the largest among FeSe-derived superconductors reported so far, indicating the great application potential.

In order to comprehensively understand the vortex pinning mechanism, the normalized vortex pinning forces $f = F_p/F_p^{\max}$, and the reduced field $h = H/H_{\max}$ for FeSe and H_x -FeSe under various temperatures are depicted in Figs. 3(a) and (b), correspondingly. Here H_{\max} is determined by the peak of the magnetic field, and F_p^{\max} represents the maximum pinning force. The F_p was calculated by the formula $F_p = \mu_0 H \times J_c$. Normally in cuprates and IBSs, $h^* = H/H_{\text{irr}}$ was commonly used for f_p data calculation [45, 46]. However, considering the difficulty in the determination of H_{irr} in high- T_c superconductors, here f_p data were converted using the reduction field $h = H/H_{\max}$. The Dew-Hughes model [47] gives several pinning mechanisms, such as $\Delta\kappa$ pinning, normal point pinning, and surface pinning. There is a certain direct functional relationship between the vortex pinning force density and reduced field h at different temperatures. In a certain temperature range, if h is consistent with one of the below equations, it means that the corresponding pinning mechanism is dominant. Different pinning mechanisms are respectively corresponding to the following equations:

$$f_p = \frac{9}{4}h(1 - h/3)^2 \quad \text{for normal point pinning,} \quad (1)$$

$$f_p = \frac{25}{16}h^{1/2}(1 - h/5)^2 \quad \text{for surface pinning.} \quad (2)$$

$$f_p = 3h^2(1 - 2h/3) \quad \text{for } \Delta\kappa \text{ pinning,} \quad (3)$$

As shown in Fig. 3(a), f_p of pristine FeSe can be well fitted by Eq. (1) from 2 to 6 K, suggesting that the pinning mechanism is dominated by the normal point pinning. In contrast, H_x -FeSe in Fig. 3(b) is well described by Eq. (2), indicating dominance of the surface pinning, as observed in FeS [48], $(\text{Li}_{1-x}\text{Fe}_x)\text{OHFeSe}$ [25] and $\text{Li}_x(\text{NH}_3)_y\text{Fe}_2\text{Te}_{1.2}\text{Se}_{0.8}$ single crystals [30]. This result suggests that H^+ protonation introduces surface-like pinning centers, which results in the enhancement of J_c and F_p . It is noteworthy that f_p is affected by flux creep and starts to deviate after H_{\max} , especially for pristine FeSe. Such deviation implicates that flux creep appears and become dominant at high magnetic fields. Similar results were also found in $\text{YBa}_2\text{Cu}_3\text{O}_{7-\delta}$ [46] and some other IBSs [45, 49].

Fig. 4(a) presents the variation of resistivity with temperature for H_x -FeSe single crystal under different magnetic fields for $H \parallel c$. A rounded feature of transition curve at T_c^{onset} clearly hints the existence of strong SC fluctuation. When the applied magnetic field increases, the resistivity curve at the SC transition continues to extend to lower temperatures, and the SC transition width is getting

significantly wider. Moreover, it is clearly seen that the SC transition curve shows a typical foot-like resistivity kink, while the zero resistivity keeps moving toward the low-temperatures as the magnetic field increases. Similar phenomena have also been observed in many other high- T_c superconductors, e.g., cuprates [50-52], (Li,Fe)OHFeSe [14], $\text{Li}_x(\text{NH}_3)_y\text{Fe}_2\text{Se}_2$ [7], 1111-type [51], and 12442-type IBSs [41]. This foot-like kink has been studied to be directly related to thermal fluctuations, and is responsible for the vortex motion through TAFF. As shown in Fig. 4(b), the characteristic temperature T_s of the foot-like kink is defined as the maximum value of the $(d\ln\rho/dT)^{-1}$ vs T curve. In high- T_c cuprates, such kink is normally associated with the first-order vortex lattice melting transition [50-63]. The first order transition from Abrikosov vortex lattice to vortex liquid at melting temperature T_m has been theoretically and experimentally demonstrated in a very clean system. When disorders are introduced, the vortex lattice is transformed from vortex liquid to glass. The transition temperature is labelled as T_g . Particularly in an intermediately disordered system, Worthington et al proposed that there exists a transitional sluggish vortex liquid region between T_m and T_g [52]. The vortex slush phase has the characteristic of short-range instead of long-range vortex lattice correlation. In $\text{H}_x\text{-FeSe}$ single crystals, the resistive transition curve shows a broaden feature with a typical foot-like resistive tail above zero resistivity, signifying the possible presence of a vortex slush phase with intermediate disorder. It should be noted that both T_m and T_s are the lower temperature limits of the vortex liquid phase boundary. The difference is that T_m is the crossover temperature between the Abrikosov vortex lattice and the vortex liquid in a very clean system, while T_s is the crossover temperature between the vortex slush phase and the vortex liquid in an intermediately disordered system.

In order to understand the state of vortex glass more deeply, we focus on the tail region in the framework of vortex glass theory. On the basis of this theory [55, 56], the resistivity above the glass transition temperature T_g is described by $\rho = \rho_0|T/T_g - 1|^s$, namely the resistivity should decrease with the power law relation. Here, s is a constant associated with the type of disorder, and ρ_0 is the characteristic resistivity of the normal state. When the inverse logarithmic derivative of the above equation is taken, $(d\ln\rho/dT)^{-1}$ and $(T - T_g)/s$ should be in a linear relationship. As depicted in Fig. 4(b), the characteristic temperatures T_g , T^* , and T_s are indicated by arrows. Fitting the linear regions of $(d\ln\rho/dT)^{-1}$ and T gives the values of T_g , T^* , and the estimated critical exponent s , where T_g is the lower temperature limit at which $(d\ln\rho/dT)^{-1}$ is zero. T^* represents the upper temperature limit that deviates from the linear fit. The vortex glass state exists in the region between T_g and T^* , and the resistivity curves of $\text{H}_x\text{-FeSe}$ single crystals can be well characterized by the vortex glass state. According to vortex glass theory, the estimated exponent s under different fields should reside in the range of $s \approx 2.7\sim 8.5$, based on the prediction of the three-dimensional (3D) vortex glass state [55]. For highly anisotropic $\text{SmFeAsO}_{0.85}$ single crystals [58], the vortex glass phase exhibits a more pronounced 2D-like behaviour, which possibly originates from the quasi-2D Fermi surface topology.

Next, we investigate the properties of the vortex liquid state above T_s through the magneto-transport measurements, as illustrated in Fig. 4(c). In accordance with the TAFF theory [52, 53, 55, 59], the equation $\rho(T, H) = (2\rho_c U/T)\exp(-U/T) = \rho_{0f} \exp(-U/T)$ gives a good description of the resistivity in the TAFF region, while $U(T, H) = U_0(H)(1-T/T_c)$. By substituting this into the equation above and taking the logarithm of both ends, the formula $\ln\rho(T, H) = \ln\rho_0(H) - U_0(H)/T$ is obtained. Here U is the thermally activation energy, while $U_0(H)$ is the activation energy associated with the magnetic field H , which has a hindering effect on the effective pinning. Meanwhile, $\ln\rho_0(H) = \ln\rho_{0f} + U_0(H)/T_c$. Therefore we can simplify the resistivity equation in this region by approximating the Arrhenius relation, $\ln\rho(T, H) = \ln\rho_0(H) - U_0(H)/T$. It can be seen from the above equation that $\ln\rho$ in the TAFF region has a positive linear correlation with $1/T$. The slope of this linear relationship is known to be $-U_0(H)$. According to the variation of resistivity with temperature under different magnetic fields, we depicted the Arrhenius plot of $\ln\rho$ versus $1/T$, as shown in Fig. 4(c). Two significantly different linear TAFF regions are observed in the higher and lower temperature regions, which are labelled by h and l , respectively. The intersection of the two linear fitting lines is defined as characteristic temperature T_{cr} . Based on the Arrhenius relation, we extract the field dependence of activation energy $U_0(H)$ for the higher temperature region h and the lower temperature region l , respectively, which are summarized in Fig. 4(d) in double-logarithmic scales. Obviously, $U_0(H)$ in both temperature regions can be fitted by the power law relation of $U_0(H) \propto H^{-\alpha}$. For region h , $U_0(H)$ follows a $\sim H^{0.54}$ dependence for the whole magnetic fields up to 9 T. However, $U_0(H)$ in the region l is divided into two regions with different values of power exponent α by a crossover field $H \sim 3.6$ T, i.e., $\alpha = 0.66$ for $H < 3.6$ T and $\alpha = 1.3$ for $H > 3.6$ T. It is widely accepted that such a power law dependence with $\alpha = 0.5 \sim 1$ is a characteristic of the 3D vortex matter, whereas a $\ln H$ dependence of the activation energy is often observed in two-dimensional (2D) SC systems [52, 64-66]. Thus, our observations strongly imply the 3D features for the vortices in H_x -FeSe single crystal.

The appearance of two TAFF regions in the vortex liquid state has been previously reported in some cuprates superconductors. For example, in $YBa_2Cu_3O_{7-\delta}$ thin films and $YBa_2Cu_4O_8$ single crystals [65, 66], Qiu *et al* observed a crossover in $U_0(H)$ from an $H^{-\alpha}$ behaviour at low temperatures to $\ln H$ at high temperatures, which can be interpreted by the change of the dimensionality of the vortices from a 3D line liquid to a 2D liquid. However, our results reveal that $U_0(H)$ displays an $H^{-\alpha}$ behaviour in both temperature regions h and l , so the change of the dimensionality of the vortices is unlikely to account the crossover observed in H_x -FeSe single crystal. According to the plastic flow model [67, 68], the vortices are plastically deformed and entangled, which results in the form of $U_0(H) \propto H^{0.5}$ for the plastic pinning. Hence, the $H^{-\alpha}$ behaviour with $\alpha = 0.54$ in the high temperature region h may be due to the strong plastic pinning. For the low temperature region l , $U_0(H)$ displays two regions well separated by a crossover field with $\alpha = 0.66$ for $H < 3.6$ T and $\alpha = 1.3$ for $H > 3.6$ T. Typically, $\alpha \sim 1$ has been commonly observed in some high- T_c cuprates and IBSs [69, 70] and is generally

interpreted as an evidence for collective pinning of vortices at high magnetic fields. For $H < 3.6$ T, the value $\alpha = 0.66$ is somewhat higher than that expected for plastic pinning, which may be due to the coexistence of plastic pinning and collective pinning. With increasing magnetic fields, the collective pinning is dominant, corresponding to the value of $\alpha = 1.3$. In addition, it is noted that the magnitude of $U_0(H)$ in the high temperature region h is larger than that of the low temperature region l , which has also been observed in some cuprates superconductors [65, 66]. One possible reason is that, as the temperature increases, due to the enhanced thermal fluctuation, the vortex liquid becomes more entangled. Consequently, the entanglement increases the viscosity of vortex liquid and results in a larger $U_0(H)$ in the high temperature region h . Certainly, further experiments are needed to verify this interpretation. Moreover, it has also been proposed that the values of power exponent α are intimately related to the type of defects that dominate the flux pinning behaviours. Typically, the planar defects are responsible for $\alpha = 0.5$ and the point defects are responsible for $\alpha = 1$ [41, 55, 64]. From this point of view, the obtained $\alpha = 0.54$ and $\alpha = 0.66$ in the high temperature region h and low temperature region l , respectively, are close to 0.5, implying that the planar defects may play an important role on the flux pinning, which is consistent with the surface pinning mechanism that is derived from the scaling of pinning force mentioned above. In the low temperature region l , we consider that a new kind of pinning center associated with point defects will be formed with increasing magnetic field and result in the larger value of $\alpha = 1.34$ at high magnetic fields.

Finally, based on the results obtained above, we construct the vortex phase diagram for H_x -FeSe single crystal, as shown in Fig. 5. The upper critical field H_{c2} is the dividing line between the normal state and the vortex liquid state. The vortex liquid state between H_{c2} and T_s is divided into region I and region II with different dissipation mechanisms governed by TAFF. With decreasing temperature, the vortex liquid-solid phase transition can be classified as several specific regions, consisting of two different kinds of transitions. The first one is called as the vortex slush transition at T_s , below which the system with intermediate disorder enters the vortex slush state with short-range lattice correlation. When the temperature is further reduced, a vortex glass critical region between T^* and T_g , where the resistivity can be described by the vortex glass theory, appears, and finally the system enters the vortex glass state below T_g .

4. Summary

To sum up, we systematically studied the J_c and vortex dynamics of H_x -FeSe single crystals. T_c of the H_x -FeSe single crystal is dramatically increased to 44 K with a bulk SC property. At 4 K, the value of J_c for H_x -FeSe is significantly enhanced by two orders of magnitude compared with 1.1×10^4 A/cm² of pristine FeSe, exceeding 1.3×10^6 A/cm². Comparing the vortex pinning characteristics, the pinning mechanism of H_x -FeSe is well described by surface pinning, while pristine FeSe is dominated by strong point-like pinning. The foot-like kink observed in the ρ - T curves of H_x -FeSe is related to the

vortex slush phase, and exhibits short-range correlation of vortex lattice. The flux pinning is governed by varying types of defects at different magnetic fields, which leads to a change in the activation energies. The detailed study of the vortex phase transition provides abundant information for the vortex phase diagram of H_x -FeSe single crystals. High- T_c H_x -FeSe single crystals show a significant enhancement of J_c , indicating the great application potential.

Acknowledgements

This work was supported by the National Key R&D Program of China (Grant No. 2018YFA0704300), the Strategic Priority Research Program (B) of the Chinese Academy of Sciences (Grant No. XDB25000000), the National Natural Science Foundation of China (Grants No. U1932217 and No. 11674054).

References

- [1] Hsu F-C, Luo J-Y, Yeh K-W, Chen T-K, Huang T-W, Wu P M, Lee Y-C, Huang Y-L, Chu Y-Y, Yan D-C and Wu M-K 2008 *Proc. Natl. Acad. Sci. U.S.A.* **105** 14262
- [2] McQueen T M, Williams A J, Stephens P W, Tao J, Zhu Y, Ksenofontov V, Casper F, Felser C and Cava R J 2009 *Phys. Rev. Lett.* **103** 057002
- [3] Ying T P, Chen X L, Wang G, Jin S F, Zhou T T, Lai X F, Zhang H and Wang W Y 2012 *Sci. Rep.* **2** 426
- [4] Ding X, Fang D, Wang Z, Yang H, Liu J, Deng Q, Ma G, Meng C, Hu Y and Wen H H 2013 *Nat. Commun.* **4** 1897
- [5] Guo J, Jin S, Wang G, Wang S, Zhu K, Zhou T, He M and Chen X 2010 *Phys. Rev. B* **82** 180520
- [6] Zhang A M, Xia T L, Liu K, Tong W, Yang Z R and Zhang Q M 2013 *Sci. Rep.* **3** 1216
- [7] Sun S, Wang S, Yu R and Lei H 2017 *Phys. Rev. B* **96** 064512
- [8] Ying T, Chen X, Wang G, Jin S, Lai X, Zhou T, Zhang H, Shen S and Wang W 2013 *J. Am. Chem. Soc.* **135** 2951
- [9] Zheng L, Miao X, Sakai Y, Goto H, Uesugi E, Eguchi R, Nishiyama S, Sugimoto K, Fujiwara A and Kubozono Y 2016 *Phys. Rev. B* **93** 104508
- [10] Li H, Wang Y, Yang X, Taguchi T, Zhi L, Goto H, Eguchi R, Ishii H, Liao Y F and Kubozono Y 2020 *J. Phys. Condens. Matter.* **32** 395704
- [11] Scheidt E W, Hathwar V R, Schmitz D, Dunbar A, Scherer W, Mayr F, Tsurkan V, Deisenhofer J and Loidl A 2012 *Eur. Phys. J. B* **85** 279
- [12] Shahi P, Sun J P, Wang S H, Jiao Y Y, Chen K Y, Sun S S, Lei H C, Uwatoko Y, Wang B S and Cheng J G 2018 *Phys. Rev. B* **97** 020508
- [13] Lu X F, Wang N Z, Wu H, Wu Y P, Zhao D, Zeng X Z, Luo X G, Wu T, Bao W, Zhang G H, Huang F Q, Huang Q Z and Chen X H 2015 *Nat. Mater.* **14** 325
- [14] Dong X, Jin K, Yuan D, Zhou H, Yuan J, Huang Y, Hua W, Sun J, Zheng P, Hu W, Mao Y, Ma M, Zhang G, Zhou F and Zhao Z 2015 *Phys. Rev. B* **92** 064515
- [15] Topping C V, Kirschner F K K, Blundell S J, Baker P J, Woodruff D N, Schild F, Sun H and Clarke S J 2017 *Phys. Rev. B* **95** 134419
- [16] Lin H, Xing J, Zhu X, Yang H and Wen H-H 2016 *Sci. China-Phys. Mech. Astron.* **59** 657404
- [17] Shi M Z, Wang N Z, Lei B, Shang C, Meng F B, Ma L K, Zhang F X, Kuang D Z and Chen X H 2018 *Phys. Rev. Mater.* **2** 074801
- [18] Gao Z, Zeng S, Zhu B, Li B, Hao Q, Hu Y, Wang D and Tang K 2018 *Sci. China Mater.* **61** 977
- [19] Sun J P, Shi M Z, Lei B, Xu S X, Uwatoko Y, Chen X H and Cheng J G 2020 *EPL-Europhys. Lett.* **130** 67004
- [20] Lei B, Cui J H, Xiang Z J, Shang C, Wang N Z, Ye G J, Luo X G, Wu T, Sun Z and Chen X H 2016 *Phys. Rev. Lett.* **116** 077002
- [21] Miyakawa T, Shiogai J, Shimizu S, Matsumoto M, Ito Y, Harada T, Fujiwara K, Nojima T, Itoh Y, Aida T, Iwasa Y and Tsukazaki A 2018 *Phys. Rev. Mater.* **2** 031801

- [22] Ying T P, Wang M X, Wu X X, Zhao Z Y, Zhang Z Z, Song B Q, Li Y C, Lei B, Li Q, Yu Y, Cheng E J, An Z H, Zhang Y, Jia X Y, Yang W, Chen X H and Li S Y 2018 *Phys. Rev. Lett.* **121** 207003
- [23] Saito Y, Kasahara Y, Ye J, Iwasa Y and Nojima T 2015 *Science* **350** 409
- [24] Zheng L, Miao X, Sakai Y, Izumi M, Goto H, Nishiyama S, Uesugi E, Kasahara Y, Iwasa Y and Kubozono Y 2015 *Sci. Rep.* **5** 12774
- [25] Yi X, Qin L, Xing X, Lin B, Li M, Meng Y, Xu M and Shi Z 2020 *J. Phys. Chem. Solids* **137** 109207
- [26] Li D, Yuan J, Shen P, Xi C, Tian J, Ni S, Zhang J, Wei Z, Hu W, Li Z, Yu L, Miao J, Zhou F, Pi L, Jin K, Dong X and Zhao Z 2019 *Supercond. Sci. Technol.* **32** 12LT01
- [27] Lei H and Petrovic C 2011 *Phys. Rev. B* **84** 212502
- [28] Liu Y, Xing Q, Dennis K W, McCallum R W and Lograsso T A 2012 *Phys. Rev. B* **86** 144507
- [29] Sun Y, Shi Z and Tamegai T 2019 *Supercond. Sci. Technol.* **32** 103001
- [30] Wang S, Sun S and Lei H 2017 *Supercond. Sci. Technol.* **30** 115005
- [31] Cui Y, Zhang G, Li H, Lin H, Zhu X, Wen H-H, Wang G, Sun J, Ma M, Li Y, Gong D, Xie T, Gu Y, Li S, Luo H, Yu P and Yu W 2018 *Sci. Bull.* **63** 11
- [32] Cui Y, Hu Z, Zhang J-S, Ma W-L, Ma M-W, Ma Z, Wang C, Yan J-Q, Sun J-P, Cheng J-G, Jia S, Li Y, Wen J-S, Lei H-C, Yu P, Ji W and Yu W-Q 2019 *Chin. Phys. Lett.* **36** 077401
- [33] Zhang H, Rousuli A, Shen S, Zhang K, Wang C, Luo L, Wang J, Wu Y, Xu Y, Duan W, Yao H, Yu P and Zhou S 2020 *Sci. Bull.* **65** 188
- [34] Meng Y, Xing X, Yi X, Li B, Zhou N, Li M, Zhang Y, Wei W, Feng J, Terashima K, Takano Y, Sun Y and Shi Z 2022 *Phys. Rev. B* **105** 134506
- [35] Sun Y, Pyon S, Tamegai T, Kobayashi R, Watashige T, Kasahara S, Matsuda Y and Shibauchi T 2015 *Phys. Rev. B* **92** 144509
- [36] Sun Y, Pyon S, Tamegai T, Kobayashi R, Watashige T, Kasahara S, Matsuda Y, Shibauchi T and Kitamura H 2015 *Appl. Phys. Express* **8** 113102
- [37] Sun Y, Pyon S and Tamegai T 2016 *Phys. Rev. B* **93** 104502
- [38] Prozorov R, Ni N, Tanatar M A, Kogan V G, Gordon R T, Martin C, Blomberg E C, Prommaphan P, Yan J Q, Bud'ko S L and Canfield P C 2008 *Phys. Rev. B* **78** 224506
- [39] Haberkorn N, Miura M, Maiorov B, Chen G F, Yu W and Civale L 2011 *Phys. Rev. B* **84** 094522
- [40] Salem-Sugui S, Ghivelder L, Alvarenga A D, Cohen L F, Yates K A, Morrison K, Pimentel J L, Luo H, Wang Z and Wen H-H 2010 *Phys. Rev. B* **82** 054513
- [41] Xing X, Yi X, Li M, Meng Y, Mu G, Ge J-Y and Shi Z 2020 *Supercond. Sci. Technol.* **33** 114005
- [42] Xing X, Li Z, Veshchunov I, Yi X, Meng Y, Li M, Lin B, Tamegai T and Shi Z 2019 *New J. Phys.* **21** 093015
- [43] Sun Y, Taen T, Yamada T, Tsuchiya Y, Pyon S and Tamegai T 2015 *Supercond. Sci. Technol.* **28** 044002
- [44] Bean C P 1964 *Rev. Mod. Phys.* **36** 31
- [45] Li M, Chen L, You W-L, Ge J and Zhang J 2014 *Appl. Phys. Lett.* **105** 192602
- [46] Klein L, Yacoby E R, Yeshurun Y, Erb A, Muller-Vogt G, Breit V V and Wuhl H 1994 *Phys. Rev. B* **49** 4403
- [47] Dew-Hughes D 2006 *Philos. Mag.* **30** 293
- [48] Wang A, Wu L, Ivanovski V N, Warren J B, Tian J, Zhu Y and Petrovic C 2016 *Phys. Rev. B* **94** 094506
- [49] Lin B, Meng Y, Li M, Feng J, Yi X, Xing X and Shi Z 2020 *J. Alloys Compd.* **819** 153017
- [50] Kwok W K, Fleshler S, Welp U, Vinokur V M, Downey J, Crabtree G W and Miller M M 1992 *Phys. Rev. Lett.* **69** 3370
- [51] Zhigadlo N D, Katrych S, Weyeneth S, Puzniak R, Moll P J W, Bukowski Z, Karpinski J, Keller H and Batlogg B 2010 *Phys. Rev. B* **82** 064517
- [52] Qiu X G, Zhao B R, Guo S Q, Zhang J R, Li L, Ichikawa F, Nishizaki T, Fukami T, Horie Y and Aomine T 1993 *Phys. Rev. B* **47** 14519
- [53] Safar H, Gammel P L, Bishop D J, Mitzi D B and Kapitulnik A 1992 *Phys. Rev. Lett.* **68** 2672
- [54] Kwok W K, Fendrich J, Fleshler S, Welp U, Downey J and Crabtree G W 1994 *Phys. Rev. Lett.* **72** 1092

- [55] Blatter G, Feigel'man M V, Geshkenbein V B, Larkin A I and Vinokur V M 1994 *Rev. Mod. Phys.* **66** 1125
- [56] Fisher D S, Fisher M P and Huse D A 1991 *Phys. Rev. B* **43** 130
- [57] Wagner P, Frey U, Hillmer F and Adrian H 1995 *Phys. Rev. B* **51** 1206
- [58] Lee H-S, Bartkowiak M, Kim J S and Lee H-J 2010 *Phys. Rev. B* **82** 104523
- [59] Palstra T T, Batlogg B, van Dover R B, Schneemeyer L F and Waszczak J V 1990 *Phys. Rev. B* **41** 6621
- [60] Eltsev Y, Holm W and Rapp O 1994 *Phys. Rev. B* **49** 12333
- [61] Darminto D, Menovsky A A and Tjia M O 2003 *Phys. Rev. B* **67** 012503
- [62] Wang C, He T, Han Q, Fan C, Tang Q, Chen D, Lei Q, Sun S, Li Y and Yu B 2021 *Supercond. Sci. Technol.* **34** 055001
- [63] Wang C, He T, Chen D, Zhang J, Fan C, Tang Q, Dong C, Tu Y, Yu B and Ma Y 2021 *Supercond. Sci. Technol.* **34** 115020
- [64] Zou X W, Wang Z H, Chen J L and Zhang H 2001 *Physica C Supercond.* **356** 31
- [65] Qiu X G, Wuyts B, Maenhoudt M, Moshchalkov V V and Bruynseraede Y 1995 *Phys. Rev. B* **52** 559
- [66] Qiu X G, Moshchalkov V V and Bruynseraede Y 1998 *Phys. Rev. B* **58** 8826
- [67] Vinokur V M, Feigel'man M V, Geshkenbein V B and Larkin A I 1990 *Phys. Rev. Lett.* **65** 259
- [68] Kierfeld J, Nordborg H and Vinokur V M 2000 *Phys. Rev. Lett.* **85** 4948
- [69] McHenry M E, Simizu S, Lessure H, Maley M P, Coulter J Y, Tanaka I I and Kojima H 1991 *Phys. Rev. B* **44** 7614
- [70] Xing X, Li Z, Yi X, Feng J, Xu C, Zhou N, Meng Y, Zhang Y, Pan Y, Qin L, Zhou W, Zhao H and Shi Z 2018 *Sci. China-Phys. Mech. Astron.* **61** 127406

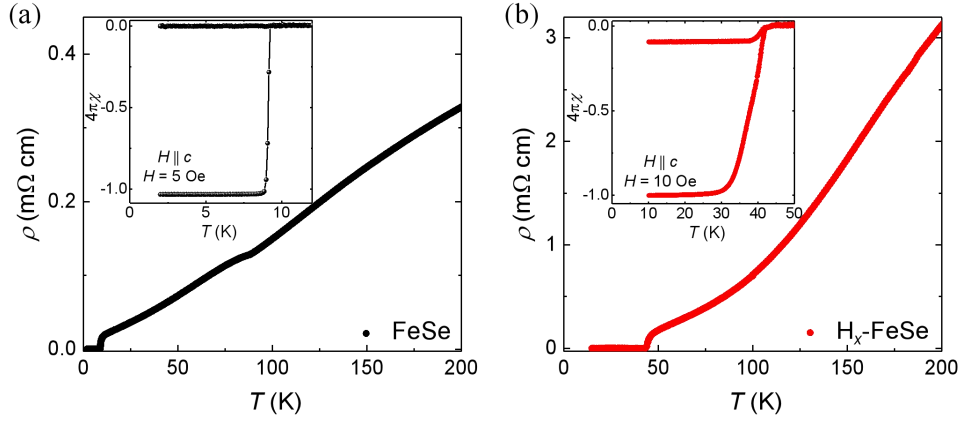
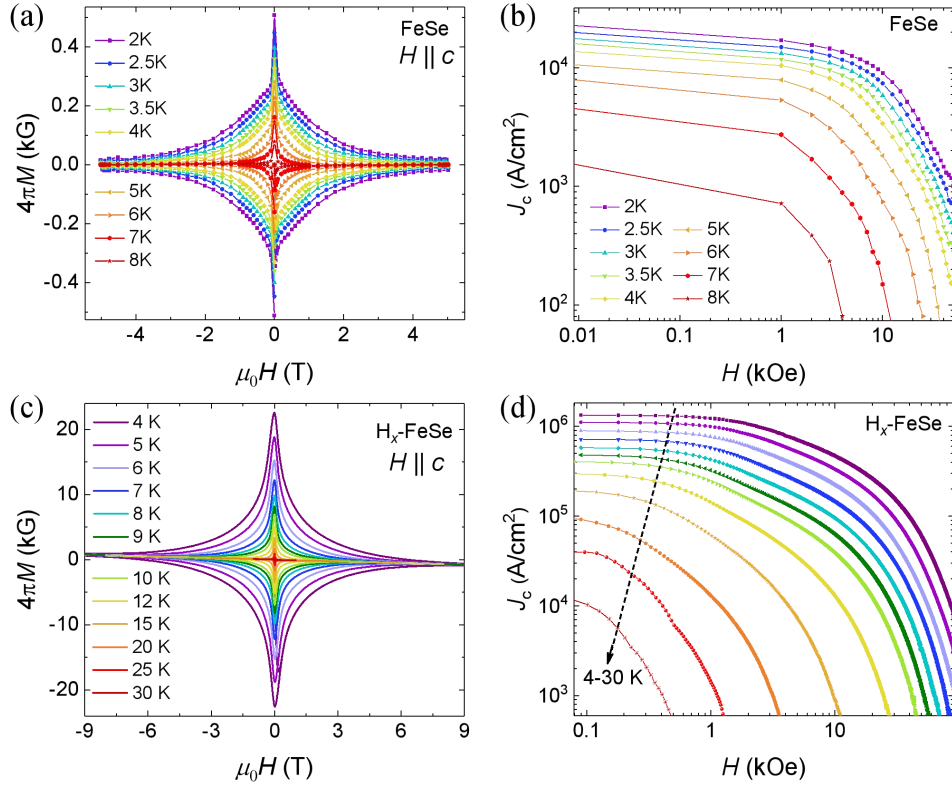


Fig. 1. (a) Temperature dependence of the electrical resistivity of FeSe single crystal. The inset shows the temperature dependences of ZFC and FC magnetizations for $H \parallel c$ under 5 Oe. (b) Temperature dependence of the electrical resistivity of H_x -FeSe single crystal. The inset shows the temperature dependences of ZFC and FC magnetizations for $H \parallel c$ under 10 Oe.



Figs. 2. MHLs at different temperatures for $H \parallel c$ and corresponding magnetic field dependence of J_c , derived from the Bean model ranging from 2 to 8 K for FeSe single crystal (a and b), and 4–30 K for optimal H_x -FeSe single crystal (c and d).

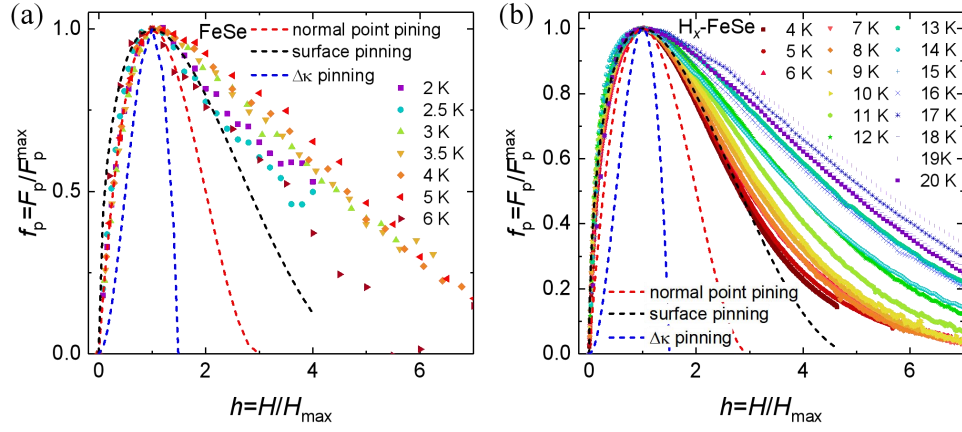


Fig. 3. Normalized flux pinning force $f = F_p/F_p^{\max}$ as a function of the reduced field $h = H/H_{\max}$ at different temperatures for (a) FeSe single crystal (b) H_x -FeSe single crystal.

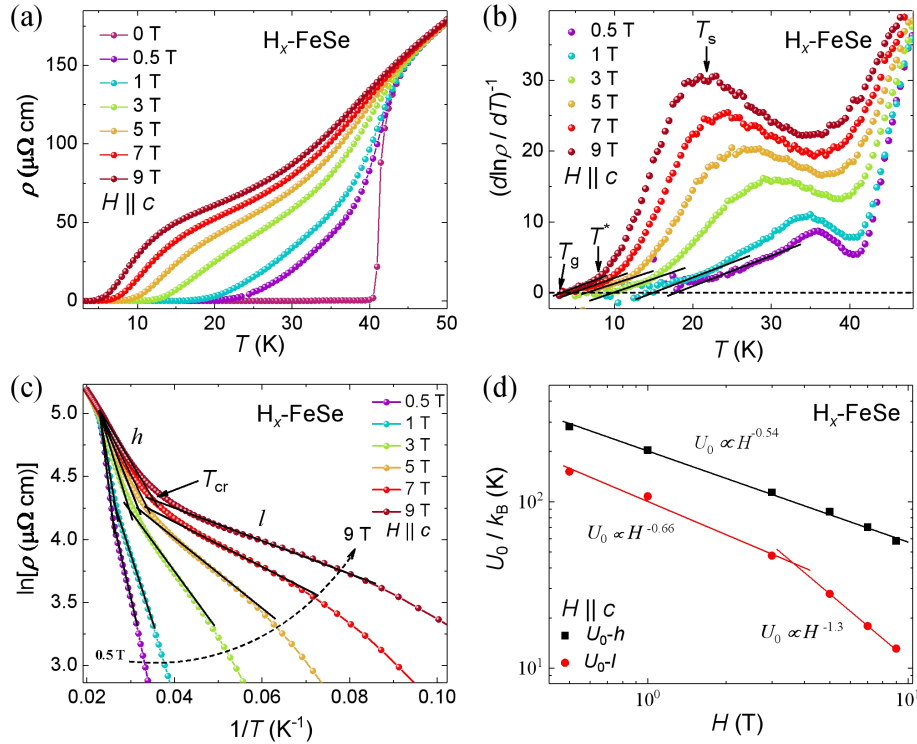


Fig. 4. H_x -FeSe single crystal (a) Resistivity as a function of temperature for magnetic fields parallel to c -axis up to 9 T. (b) Temperature dependence of $(d \ln \rho / dT)^{-1}$ for varying magnetic fields ranging within 9 T for $H \parallel c$, with the associated characteristic temperatures marked with arrows. The dashed line is guide to the eye. (c) Arrhenius plot of the resistive transitions at varying magnetic fields. Two significantly different linear TAFF regions are fitted by black lines in the higher and lower temperature regions, which are labelled by h and l respectively. The intersection of the two linear fitting lines is defined as characteristic temperature T_{cr} . (d) The function relation between activation energy $U_0(H)$ and magnetic field H in double-logarithmic scales.

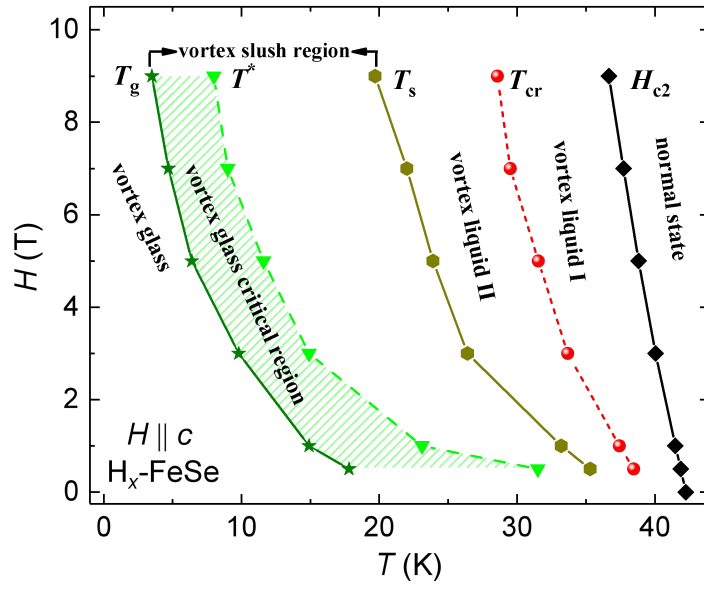


Fig. 5. Vortex phase diagram of optimal H_x -FeSe single crystal with $H \parallel c$.